Cellulose
https://doi.org/10.1007/s10570-025-06427-9

ORIGINAL RESEARCH

Microextrusion-based 3D printing for the free-shape deposition of functional cellulose-based electronic materials

Enrico D. Lemma · Vincenzo Ranieri · Chiara Coricciati · Alessio Bucciarelli · Dalila Fontana · Pamela Mozetic · Marcella Trombetta · Giuseppe Gigli · Alberto Rainer

Received: 19 September 2024 / Accepted: 2 February 2025

Abstract Cellulose is the most abundant renewable biomaterial, featuring a wide range of applications. In the form of aqueous suspension of microfibrils, it is also highly processable, which has opened new doors to a number of industrial applicative scenarios. In particular, extrusion 3D printing enables the free-form fabrication of stable cellulose-based constructs with applications, among others, in flexible electronics. However, most of these devices still rely on costly metal elements and show a relatively low cellulose fraction, mainly associated to the substrate. Here, we applied an optimization strategy to the microextrusion-based 3D printing of microfibrillated cellulose/hydroxypropylcellulose composites, which were further modified by the addition of nanocarbon and doped ZnS powders, thus endowing the materials with conductive and electroluminescent properties, respectively. The formulations were also demonstrated to be non-cytotoxic and, in principle, suitable for application in contact with living matter. In conclusion, we fabricated and integrated cellulose-based 3D printed materials with a broad applicative potential ranging from flexible electronics to biocompatible devices, potentially leading to the development of a new class of cellulose-based (bio)electronic components with reduced environmental impact.

Enrico D. Lemma and Vincenzo Ranieri have contributed equally to this work.

Supplementary Information The online version contains supplementary material available at https://doi.org/10.1007/s10570-025-06427-9.

E. D. Lemma (✉) · V. Ranieri · D. Fontana · A. Rainer
Department of Engineering, Università Campus Bio-Medico di Roma, Via Álvaro del Portillo 21, 00128 Rome, Italy
e-mail: e.lemma@unicampus.it

E. D. Lemma · C. Coricciati · A. Bucciarelli · P. Mozetic · G. Gigli · A. Rainer
Institute of Nanotechnology (NANOTEC), National Research Council, Via Monteroni, 73100 Lecce, Italy

C. Coricciati
Department of Mathematics and Physics "Ennio De Giorgi", University of Salento, Via Monteroni, 73100 Lecce, Italy

A. Bucciarelli
Department of Industrial Engineering, BIOtech Research Center, Italy and European Institute of Excellence On Tissue Engineering and Regenerative Medicine, University of Trento, Via Delle Regole 101, 38123 Trento, Italy

M. Trombetta
Department of Science and Technology for Sustainable Development and One Health, Università Campus Bio-Medico di Roma, Via Álvaro del Portillo 21, 00128 Rome, Italy

G. Gigli
Department of Experimental Medicine, University of Salento, Via Monteroni, 73100 Lecce, Italy

Published online: 10 February 2025

Keywords Microextrusion-based 3D printing · Cellulose · Process optimization · Response surface method · Functional materials

Introduction

One of the most promising materials to reduce the environmental footprint of electronic devices is native cellulose, an abundant and widely investigated (Turbak et al. 1983) natural polymer which can be extracted from a variety of plant sources (Ferrer et al. 2016; Başaran Kankılıç and Metin 2020). Indeed, cellulose can be obtained also artificially (Basu et al. 2016) or bacterially (Zhong 2020). Cellulose constitutes the main component of the plant cell wall, conferring structural stability to the plant. This suggests that cellulose is a biomaterial with strong mechanical characteristics, mainly due to its fibrillar microstructure (Nishiyama 2009). However, cellulose hygroscopicity is often exploited to prepare aqueous suspensions with the appearance of a viscous pulp, which is mechanically unstable, but endows the material with a high degree of versatility: this is demonstrated by the possibility of freely shaping microfibrillar cellulose paste, e.g., via extrusion-based techniques. The latter is a peculiar type of three-dimensional (3D) printing, in which a viscous material flows through a nozzle at controlled pressure, and the relative motion between the nozzle and an x–y-z stage leads to the layer-by-layer deposition of the material, in a virtually free-form geometry defined via software. Therefore, the suitability of cellulose pastes for 3D printing opens to their application as starting materials for novel bio-compatible, functional, flexible devices (Li et al. 2022; Iglesias-Mejuto et al. 2024). 3D shaping of microfibrillar cellulose paste can be coupled with the modification of the pulp with fillers and/or monomers (Panaitescu et al. 2007; Torvinen et al. 2017; Li et al. 2019; Maturi et al. 2023; Kwon et al. 2023; Yang et al. 2024).

In this context, a number of cellulose-based electronic devices have been produced in the last years and extensively reviewed (Fang et al. 2021; Zhao et al. 2021). Flexible electronics represent a remarkable technological advance for the development of smart devices in various fields. However, even in the most advanced cases, the basic structuring of the electronics has never changed, with electrodes mostly being realized with rare or precious elements (e.g., indium, tin, silver, etc.), and transparent components being made of synthetic polymers. Issues in materials supply, limited stocks, and difficulties in disposal/recycling of exhausted devices have induced researchers to search for alternative routes to polymeric substrates and rare metal electronics. In the case of cellulose-based devices, variously modified and processed micro- or nanofibrillated cellulose is used as flexible, transparent and biodegradable support for light-emitting diodes, sensors, etc. However, even these devices include metallic electrodes and/or multilayered structures, with cellulose constituting only a relatively small portion (Jung et al. 2015; Xu et al. 2016; Zheng et al. 2021). Instead, to the best of our knowledge, conductive, light-emitting devices based predominantly on cellulose have not been developed yet. Indeed, fully cellulose-based electronic devices would further broaden the advantages of the presently available devices, leading to a new class of fully biodegradable devices not requiring scarcely available materials (e.g., indium tin oxide, gold, etc.). In addition, the possibility to realize light-emitting devices exclusively via cellulose-based materials would, in principle, simplify the manufacturing procedures, being the whole fabrication process more sustainable in terms of costs and environmental impact.

In this work, we present a composite formulation based on microfibrillated cellulose and hydroxypropyl cellulose (HPC) which has undergone a comprehensive rheological, morphological, and mechanical characterization. We show that the material is suitable for microextrusion-based 3D printing, and that process parameters optimization leads to fine control over printing outcomes. We also show that the material can be further modified by the addition of conductive and electroluminescent phases, leading to functional materials which can be combined in a multi-material 3D printing process to produce a prototypal light-emitting device. Finally, we prove that the developed materials are biocompatible and are, in principle, suitable for applications in contact with living matter. Indeed, our optimized cellulose-based formulations show high processability via extrusion techniques and are suitable for assembling in a fully cellulose-based light-emitting device. The possibility to exploit 3D printing for all the materials involved in the fabrication of a functional device greatly simplifies fabrication procedures and positively impacts

on the adhesion of the different components of the device, which could lead to the development of 3D extrusion as a key technology for manufacturing fully cellulose-based biocompatible, flexible and sustainable electronics.

Results

Rheological characterization of microfibrillated cellulose

Commercial F-01 V microfibrillated cellulose in water (10 wt%, Fig. 1a) was firstly printed as received with a custom-built pressure-actuated micro-extrusion 3D printer (Gori et al. 2020). Under extrusion conditions, the mixture showed a clear effect of syneresis, with the water phase drastically separating from the microfibrils and being expelled from the nozzle (see Supplementary Fig. S1a). To avoid this effect, the composition of the mixture was modified by the addition of HPC as a thickener and PEGDA with Irgacure 2959 photoinitiator to make the blend photo-crosslinkable.

Table 1 summarizes the optimized composition of the microfibrillated cellulose formulation (optimized cellulose blend, OCB), which could be stably extruded at various pressures and substrate speeds (Supplementary Fig. S1b).

The rheological properties of the blend were firstly investigated (Shafiei-Sabet et al. 2012; Nechyporchuk et al. 2016). As reported in Fig. 1b, for the uncured condition, viscosity at rest was not affected by the inclusion of HPC, PEGDA and Irgacure 2959 (OCB), while an increase was reported following UV crosslinking at 405 nm (photocrosslinked OCB, P-OCB). In all conditions, a clear shear-thinning behavior was shown, but the stability of the materials was guaranteed only for shear rates $< 0.002\ s^{-1}$ (shadowed region in the shear stress vs. shear rate plots). Indeed, for higher shear rates, microfibrillated cellulose and the two blends (OCB and P-OCB) start to disaggregate. Subsequently, oscillating amplitude and frequency tests (Fig. 1c) were performed to extrapolate the storage (G') and loss (G'') moduli. As it could be expected from the appearance of the materials (i.e., a soft, but compact paste), the elastic behavior is predominant (G' $\approx$ 10 – 50 kPa), with a linear viscoelastic region (LVE) of 0.05% for microfibrillated cellulose and OCB, and of 0.09% for P-OCB. Accordingly, the elastic behavior overcomes the viscous properties at a broad range of frequencies. Finally, to simulate time-dependent structural regeneration after shearing associated to the extrusion-based 3D printing process, we performed an oscillation-rotation-oscillation test on the pastes (Fig. 1c), which showed an almost complete recovery (> 95%) of the storage modulus G' in less than 30 s after the perturbation. Syneresis of the microfibrillated cellulose paste was not detectable from this test, suggesting that the solid/liquid phase separation is reliably due to the geometrical features of the extrusion system (i.e., a syringe equipped with a blunt-tip needle, which introduces a sudden restriction to the pressure-driven flow of the microfibrillated cellulose paste). Conversely, for P-OCB, G' did not recover above 70% even after 1.5 min following perturbation, reliably due to the disruption of the crosslinked network. For this reason, photo-crosslinking of OCB should be performed only after the extrusion process.

3D printability and response surface modeling

To fine-tune the printing parameters via 3D printing, a systematic investigation was carried out. Therefore, single linear strands (2 cm long) of OCB were printed at different pressure (1200 – 2450 mbar) and speed (2 – 10 mm/s) levels, using two different blunt nozzles with 510 µm and 840 µm inner diameter (ID). To extrapolate an empirical model, a Response Surface Method (RSM) (Bucciarelli et al. 2020, 2021; Bossi et al. 2021; Gaiardo et al. 2021) was adopted, with three continuous factors being considered (A-Printing pressure, B-Printing speed and C-Nozzle diameter) (see Table 2 in Materials and Methods section).

Two yields were measured, one continuous (the strand width in micrometers) and one binary (0-not printable; 1-printable), the latter modelled with a logistic regression. These are described by Eqs. (1) and (2), respectively.

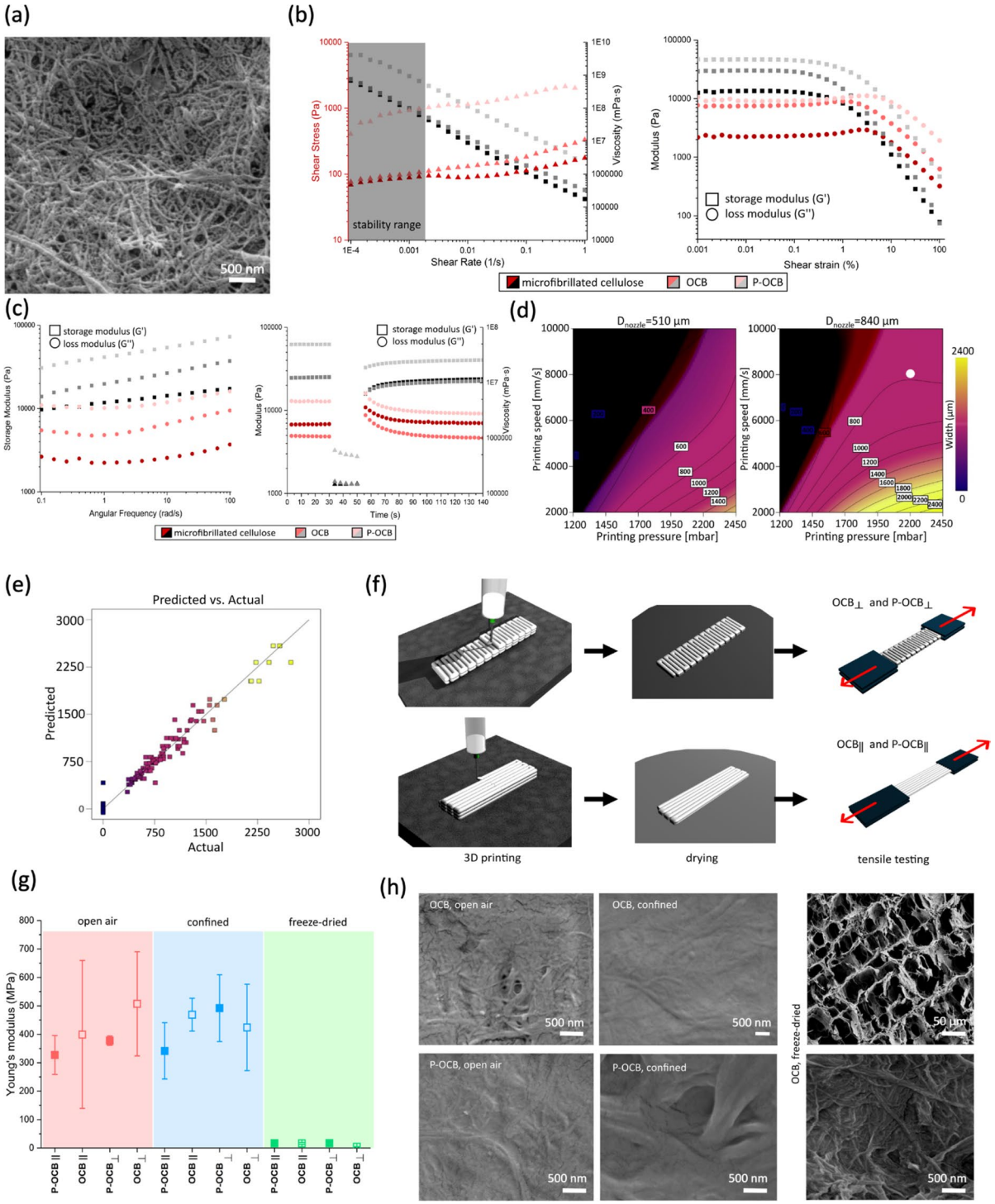
(a)
500 nm
(b)
Shear Stress (Pa)
Viscosity (mPa·s)
stability range
Shear Rate (1/s)
Modulus (Pa)
storage modulus (G')
loss modulus (G'')
Shear strain (%)
microfibrillated cellulose
OCB
P-OCB
(c)
storage modulus (G')
loss modulus (G'')
Storage Modulus (Pa)
Angular Frequency (rad/s)
Modulus (Pa)
Viscosity (mPa·s)
Time (s)
microfibrillated cellulose
OCB
P-OCB
(d)
D_nozzle=510 µm
D_nozzle=840 µm
Printing speed [mm/s]
Printing pressure [mbar]
Width (µm)
(e)
Predicted vs. Actual
Predicted
Actual
(f)
OCB⊥ and P-OCB⊥
OCB∥ and P-OCB∥
3D printing
drying
tensile testing
(g)
open air
confined
freeze-dried
Young's modulus (MPa)
P-OCB ∥
OCB ∥
P-OCB ⊥
OCB ⊥
(h)
OCB, open air
OCB, confined
P-OCB, open air
P-OCB, confined
OCB, freeze-dried
500 nm
50 µm

◂**Fig. 1** **a** SEM micrograph of F01-V cellulose; **b** rheological characterization of the F01-V cellulose, of OCB and P-OCB: viscosity (left), and amplitude tests (right); **c** frequency tests (left), and oscillation-rotation-oscillation test (right) for F01-V cellulose, OCB and P-OCB to simulate the extrusion process; **d** contour plots of the RMS model for the two nozzle IDs; **e** predicted data of the model vs. actual experimental values, showing the accuracy of the RMS model; **f** sketches of the extrusion process along different directions and tensile testing; **g** stiffness of OCB and P-OCB (840-µm blunt needle) as a function of printing direction and drying conditions; **h** SEM micrographs of OCB and P-OCB for different drying conditions

$$t(\mu m) = 6.19 \cdot 10^2 + 1.95 \cdot 10^2 A + 3.10 \cdot 10^2 B - 2.36 \cdot 10^2 C + 8.51 \cdot 10^1 AB - 1.13 \cdot 10^2 AC + \\ - 3.19 \cdot 10^2 BC - 2.02 \cdot 10^2 B^2 + 3.37 \cdot 10^2 C^2 - 4.48 \cdot 10^1 ABC - 1.46 \cdot 10^2 AB^2 + 1.32 \cdot 10^2 AC^2 + \\ + 1.94 \cdot 10^2 BC^2 + 1.33 \cdot 10^2 B^3 - 2.14 \cdot 10^2 C^3 \quad (1)$$

$$logit\left[P(printability = 1)\right] = 2.98 + 1.78\,A + 1.09 \cdot 10^1\,B - 1.01 \cdot 10^{21}\,C + 6.29 \cdot 10^{-1}\,BC + \\ - 5.01\,B^2 + 4.51\,C^2 + 9.97\,B^2C - 6.26\,BC^2 \quad (2)$$

In Fig. 1d, the contour plots for the strand width (Eq. 1) are reported for the two end point values of the nozzle ID. The surfaces derived from the logistic regression (Eq. 2) have been superimposed to the plot. In the darkened area, the printability tends to 0, while in the visible area the printability equals 1. As expected, the strand width increased with increasing the pressure and decreasing the printing speed. Predicted *vs.* actual plot (Fig. 1e) ($R^2 = 0.9613$) confirmed accurate fitting. Coefficients and corresponding F values are reported in Supplementary Tables S1–S4. Mechanical stability of OCB was also assessed by a filament printability test (Lechner et al. 2022), which showed that the formulation was compatible with the obtaining of continuous, suspended strands hanging up to 16 mm span (Supplementary Fig. S1c).

We chose to work with a minimum feature resolution (corresponding to the strand width) below 800 µm, whilst maximizing the printing speed. Hence, based on the RSM model, the printing conditions for OCB were set as follows: pressure = 2200 mbar; printing speed = 8000 µm/s; 840 µm ID nozzle (identified with a mark on the plot in Fig. 1d).

Mechanical characterization of extrudates

Mechanical properties of the extrudates were assessed to evaluate the possible range of applications for the microfibrillated-cellulose-based printable formulations. Since the overall mass percentage of water of OCB and P-OCB is approximately 90%, we hypothesized that the drying conditions of the printed specimens could play a role in the resulting mechanical strength. Therefore, we tested 3D printed samples which were either dried (i) in open air at 50 °C; (ii) under confined drying (between two glass slides) at 50 °C; or (iii) via freeze-drying. Since the easiest infill pattern is represented by parallel strands, we also investigated potential mechanical anisotropies in dried OCB and P-OCB structures. Rectangular specimens were printed with infill direction either along the length and width of the rectangle and underwent tensile testing, thus applying the load either parallelly or perpendicularly to the fiber deposition direction (indicated as $OCB_{\parallel}$, $OCB_{\perp}$, $P\text{-}OCB_{\parallel}$, and $P\text{-}OCB_{\perp}$, respectively) (Fig. 1f).

As shown in Fig. 1g, Young's modulus of the blends did not change significantly with the drying procedure, with the expected exception of freeze-dried samples, and did not show a clear dependence on the extrusion direction. This behavior could be explained by the micro-structure of the blends (SEM micrographs of Fig. 1h), since alignment pattern of cellulose microfibrils could not be observed. Freeze-drying, instead, severely affected the resulting mechanical properties, with a dramatic (approximately two orders of magnitude) reduction of the Young's modulus. This behaviour can be related to the different compactness of the blends after drying: indeed, open-air and constrained drying led to a compact, stiffer material, while the high degree

Table 1 OCB composition

Component	Relative amount (wt%)
Water	88
Microfibrillated cellulose	5
PEGDA, Mw 700 Da	5
HPC, Mw 350 kDa	1
Irgacure 2959	1

of porosity resulting from freeze drying negatively affects mechanical properties (Illa et al. 2019).

Interestingly, open-air drying of P-$OCB_{\parallel}$ showed the narrowest dispersion of stiffness measurements, thus suggesting that this configuration ensured the most reproducible manufacturing strategy. However, in general, it cannot be stated that the photocrosslinking of the blend significantly improved mechanical properties of the dried samples.

With reference to the mechanical strength of the extrudates, results are summarized in Supplementary Fig. S2. In particular, tensile strength for $OCB_{\parallel}$ blends generally showed higher values in comparison to $OCB_{\perp}$, independently of the drying conditions. Despite not influencing the Young's modulus, extrusion direction could expectedly be related to tensile strength, with specimens loaded parallelly to the fiber deposition showing higher resistance. Moreover, constrained drying further improves mechanical strength, possibly due to an increased material cohesion, which in turn can be ascribed to a slower rate of dehydration. Finally, representative cyclic loading–unloading tests were performed, to show that OCB can be mechanically stressed for at least 100 cycles maintaining its elastic properties.

Overall, the mechanical behaviour of the cellulose formulations are in agreement with comparable materials reported in literature obtained via extrusion techniques. Despite being well below the values of native cellulose (Moon et al. 2011), Young's modulus and tensile strength show relatively lower (Jonoobi et al. 2010; Sehaqui et al. 2011; Hausmann et al. 2020) or comparable (Siqueira et al. 2017) values with respect to other micro- and nanofibrillated cellulose composites, strongly depending on the composition of the matrix in which cellulose is dispersed.

Conductive formulations and electrical characterization

To prove the versatility of the microfibrillated-cellulose-based blends for obtaining functional materials, OCB was first modified by introducing increasing fractions of a conductive filler, namely Super P carbon black powder, leading to an electrically conductive blend (E-OCB, SEM micrograph shown in Fig. 2a). Expectedly, the resulting formulations demanded higher extrusion pressures compared to OCB and P-OCB (1600–3600 mbar) given their increased viscosity (Supplementary Fig. S3).

Table 2 Experimental design with the parameters for the RSM model

Coded name	Factor	Unit	Levels		Type
			D_{nozzle} 510 µm	D_{nozzle} 840 µm	
A	Printing pressure	mbar	1200	1200	Numerical
			1450	1450	
			1700	1700	
			1950	1950	
			2200	2200	
			2450	2450	
B	Printing speed	µm/s	2000	2000	Numerical
			4000	4000	
			6000	6000	
			8000	8000	
			10,000	10,000	
C	Nozzle diameter	µm	510		Numerical
			840		

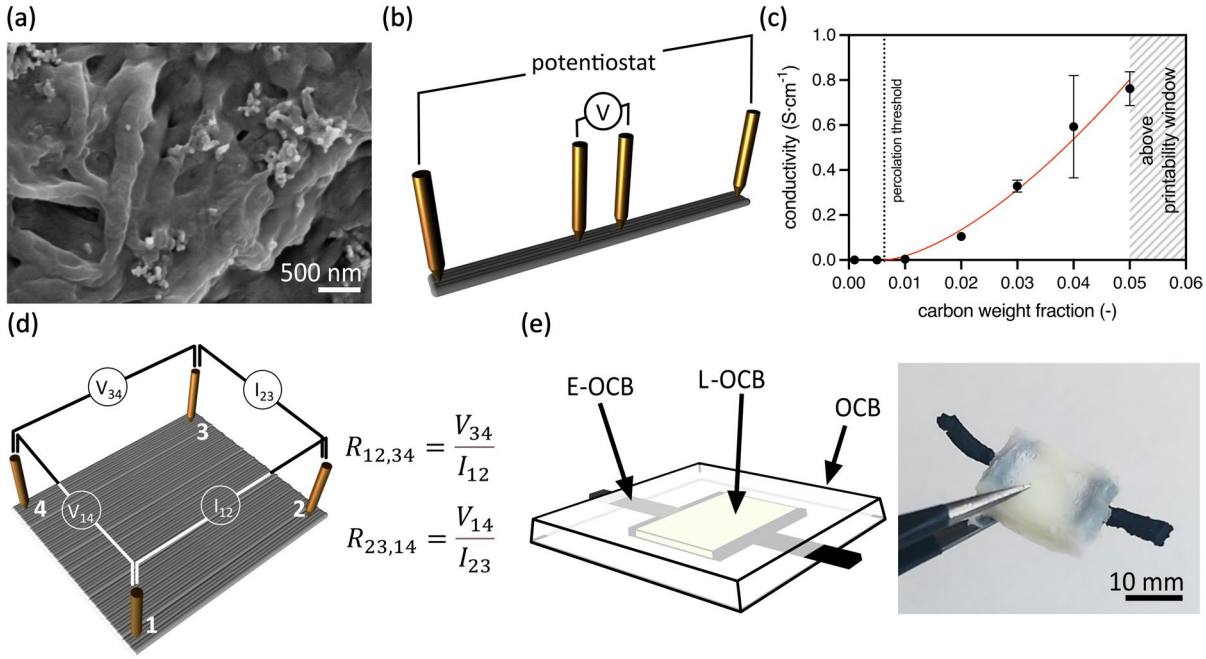

Fig. 2 **a** SEM micrograph of E-OCB, showing graphite nanometric inclusions; **b** sketch of four-terminals conductivity test setup; **c** conductivity of E-OCB as a function of carbon black fraction; **d**: sketch of surface conductivity test setup; **e** sketch (left) and macrograph (right) of a composite OCB, L-OCB and E-OCB device

A 5 wt% carbon black fraction was experimentally determined as the printability threshold, above which the formulations lose their extrudability properties. For an intermediate amount of carbon black (i.e., 3 wt%), the E-OCB blend was mechanically characterized via tensile testing. Expectedly, the Young's modulus does not increase significantly ($E = 392.8 \pm 56.9$ MPa) with respect to OCB, but a more brittle behaviour can be observed: indeed, tensile strength ($\sigma = 2.10 \pm 0.74$ MPa) and elongation at break ($\varepsilon = 0.013 \pm 0.006$ mm/mm) were both significantly lower than the respective values for OCB blend. This could be ascribed to the introduction of the carbon black powder in the homogeneous cellulose-based matrix composing OCB. The linear conductivity of extruded linear strands of E-OCB was then measured via 4-terminal technique according to the scheme in Fig. 2b. Voltage *vs.* current curves were recorded in DC for E-OCB samples at different carbon black fractions (0.1 – 5 wt%) and corresponding conductivity values were retrieved, as shown in Fig. 2c. As expected, an increase in material conductivity with increasing the carbon black content could be observed, with the formulation at 5 wt% carbon black reaching a conductivity of 0.762 S cm^{-1}. Fitting of conductivity data according to the statistical percolation theory gave an electrical percolation threshold at 0.6 wt% carbon black (fitting results are summarized in Supplementary Table S5). The obtained results are comparable to the conductivity of other cellulose-based blends with carbon fillers (e.g., carbon nanotubes) (Imai et al. 2010; Pokhrel et al. 2023), or with conductive polymers (e.g., polyaniline) (Saleh et al. 2024), despite being lower than composites realized with metal nanowires (Park et al. 2017), or PEDOT: PSS polymers (Liu et al. 2023; Jain et al. 2023). Carbon black-doped cellulose composites have also been reported, showing higher resistivity despite an increased amount of filler with respect to our formulation (Imai et al. 2010).

The influence of printing direction on conductivity was also investigated. To this aim, a surface resistance measurement was performed on square-shaped specimens featuring a dense linear infill pattern (same orientation for all layers) via the van der Pauw method, as shown in Fig. 2d: the surface conductivity shows a certain degree of anisotropy, being the resistivity

along the strands lower than the resistivity across the strands ($\rho_{23,14}/\rho_{12,34} = 1.41 \pm 0.22$).

Electroluminescent formulations and devices

After investigating the conductive properties of E-OCB, an electroluminescent material (L-OCB) was obtained by incorporation of doped ZnS electroluminescent microparticles (a SEM micrograph of the ZnS crystals and their size distribution are shown in Supplementary Fig. S4) into OCB. Upon application of a voltage in the range of 3 – 6 kV to a 10 mm × 10 mm × 2 mm 3D-printed sample, a clearly visible light in the green spectrum region was emitted (Supplementary Video 1). Expectedly, the electroluminescent effect of the phosphor is proportional to the intensity of the electric field generated between the terminals. Although the highest luminescence results reported in literature are usually obtained by exploiting transition metals or rare earth ions (Shi et al. 2017; Amela-Cortes et al. 2023), the use of CdSe/ZnS micro/nanocrystals or quantum dots enables facile inclusion in cellulose-based blends (Small and Johnston 2008; Yang et al. 2012; Pinto et al. 2014).

As a proof of concept, OCB, E-OCB and L-OCB were combined to demonstrate the feasibility of integrating different cellulose-based formulations into a functional electroluminescent device. In particular, a sandwich structure was fabricated, featuring: (i) a first lower layer of OCB; (ii) two capacitor-like plates of E-OCB connected to E-OCB wires and enclosing an emissive L-OCB layer; and (iii) an upper closing layer of OCB (Fig. 2e). Also in this case, the application of a ≈5 kV voltage induced photoemission from the L-OCB portion of the device, while the OCB layers protected the device and the E-OCB components from the surrounding environment.

Biocompatibility and scaffolds for 3D cell cultures

As a final demonstration of the wide variety of application fields for the proposed microfibrillated cellulose-based formulations, we investigated the biocompatibility of OCB, P-OCB and E-OCB materials. Indeed, cellulose is a highly biocompatible material (Hickey and Pelling 2019), and the inclusion of fillers usually does not hamper growth, migration and proliferation of cells when these are cultured in presence of

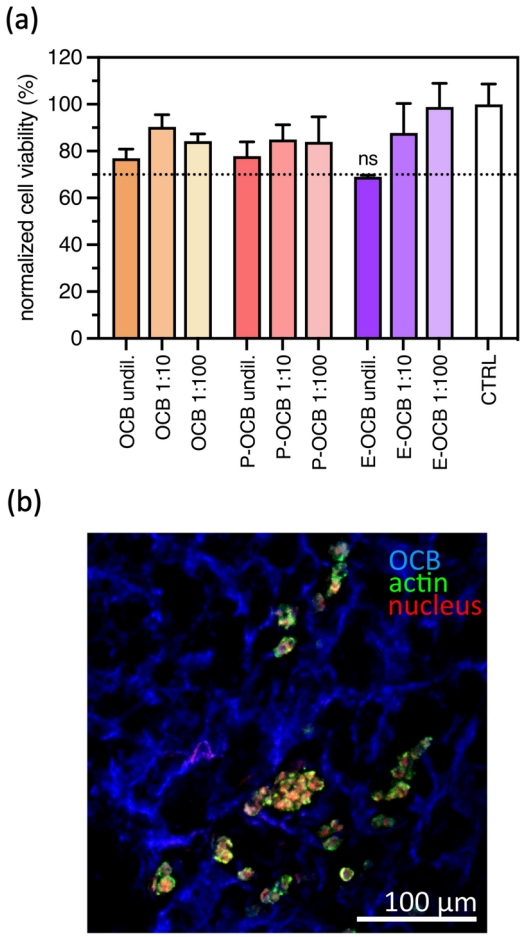

Fig. 3 **a** Results of MTT assay for OCB, P-OCB and E-OCB performed on SK-MEL-2 human melanoma cell line; **b** Confocal micrograph of SK-MEL-2 cells cultured on OCB scaffold

conductive blends (Kuzmenko et al. 2018). Biocompatibility was assessed according to the ISO 10993–5 standard (ISO 2003): freeze-dried specimens were soaked in cell culture medium, then the eluates were supplemented at different titers to the SK-MEL-2 cell line. Cell viability was measured via MTT assay (Fig. 3a). All formulations were not cytotoxic, showing a cell viability higher than the threshold of 70% at all concentrations (excluding undiluted E-OCB, although the difference was not significant as per one-sample t-test), in agreement with conductive cellulose-based formulations reported in literature (Fu et al. 2020; Wang et al. 2020; Salehi et al. 2021). To verify whether OCB could serve as a scaffold for 3D cell culture, freeze-dried samples were rehydrated in

culture medium and then incubated with SK-MEL-2 cells for 72 h. As shown in Fig. 3b, the porous network enabled cell adhesion to the inner structure of the scaffold.

Conclusion

We have successfully optimized a palette of 3D-printable materials based on microfibrillated cellulose showing different mechanical, electrical and optical properties. Insulating cellulose/HPC formulations (OCB) could be extruded over a broad range of printing pressures and speeds (as thoroughly described by a RSM model), showing Young's modulus values ranging between 325 and 525 MPa, depending on the post-processing condition. The addition of small percentages of carbon black powder increased the conductivity of the formulation to 0.3 – 0.8 S cm^{-1} without compromising the printability, while the inclusion of photoluminescent crystals enabled photoemission. Taken together, our results show that it is possible to integrate the formulated blends into a single functional electroluminescent structure. Indeed, it is the first time to the best of our knowledge that an emissive device is realized which (i) is exclusively composed of cellulose-based materials and (iii) can be wholly printed by in a single, multi-material 3D printing process. However, high currents associated to the considerable voltages needed to induce electroluminescence were sometimes responsible for local overheating of the OCB/E-OCB interface, thus dramatically reducing the emissive response of the device. Therefore, further optimization steps are needed to develop a L-OCB formulation working at lower voltages (e.g., by using more efficient electroluminescent crystals). Together with our finding that OCB and E-OCB are biocompatible, it is possible to envision that our work will help the development of a new class of full-cellulose-based environmentally friendly solutions for (bio)-electronic devices.

Materials and Methods

Chemicals and OCB preparation

EXILVA F01-V microfibrillated cellulose was a kind gift from Borregaard AS (Norway). Hydroxypropyl cellulose (HPC, MW 370 kDa), poly(ethylene glycol) diacrylate (PEGDA, MW 700 Da), and Irgacure 2959 (IC2959) were purchased from Merck KGaA (Germany). All other reagents were purchased from Merck KGaA, unless specified. For a typical OCB batch, 100 mg of HPC were added to 4.4 mL of deionized water and stirred for 90 min. Then, 500 mg of PEGDA were added, and further mixed for 15 min. Subsequently, 5 g of F01-V cellulose were added to the mixture, together with 100 mg of IC2959. The blend was homogenized in a Thinky ARE-250 planetary mixer (Thinky, USA) for 1 min, followed by a 30 s degassing step.

Extrusion-based 3D printing

A custom-made 3D printing system was used (Gori et al. 2020), featuring a fixed column design with a dispensing head (moving along z) and an x–y baseplate. The dispensing head hosted a 3 mL fluid dispensing syringe (Optimum, Nordson EFD, USA) fed by a pressure controller (OB1-MK3, Elveflow, France; 0–8000 mbar range). All specimens and devices were printed on 24 × 50 mm (length x width) microscope coverslips. In the case of P-OCB, UV irradiation (330 mJ/cm^2 at 405 nm) was carried out after covering the exposed surface with a coverslip to prevent evaporation. P-OCB was exposed immediately after mixture preparation or stored in a dark environment to avoid unintended photopolymerization. The filament printability test was performed according to a procedure described elsewhere (Lechner et al. 2022).

Rheology

Rheological properties of microfibrillated cellulose, OCB and P-OCB were investigated on a MCR 302 rheometer (Anton Paar, Austria), using a 25-mm diameter plate-plate configuration with a 1 mm gap at 25 °C. For viscosity investigations at very low shear rates ($\dot{\gamma} \approx 0.0001$ s^{-1}), the "steady state" sampling method was set to avoid artifacts. For amplitude sweep tests, oscillation was set to $\omega = 10$ rad/s; for frequency sweeps, a value of shear strain $\gamma = 0.05\%$ (within the LVE region) was chosen for all cases. For oscillation-rotation-oscillation probing, samples were firstly tested at $\gamma = 0.05\%$, $\omega = 10$ rad/s for 30 s, then mechanical stress was imposed via rotation at $\dot{\gamma} = 1$ s^{-1}

for 20 s, and finally G' and G'' recovery was investigated at $\gamma = 0.05\%$, $\omega = 10$ rad/s for 90 s.

Scanning electron microscopy

SEM micrographs were obtained with a Sigma 300 VP microscope (Zeiss, Germany) operated at 5 kV on specimens mounted on aluminum stubs and coated with 7 nm of sputtered gold (CCU-010 LV, Safematic, Switzerland).

RSM modeling

To compile the RSM model, single 20-mm-long linear strands of OCB were extruded at various printing pressure and speed levels, using two distinct blunt end tips with different ID. The overall Design of Experiment is reported in Table 2.

Extruded strands were immediately viewed under an inverted microscope (Ti-E, Nikon Instruments, Japan) and strand width was measured using ImageJ software suite (v.1.52) (Huang et al. 2012).

The whole statistical analysis was performed using R programming language (Li et al. 2022; Iglesias-Mejuto et al. 2024). The model was built by selecting the significantly relevant factors, tested by analysis of variance (ANOVA). The significant level was assigned as follows: $p \leq 0.1$ (·), $p \leq 0.05$ (*), $p \leq 0.01$ (**), $p \leq 0.001$ (***). The complete model for strand width is reported in Eq. 3.

$$\begin{aligned} f(Y) = {} & c_0 + c_1A + c_2B + c_2AB + c_3A^2 + c_4B^2 + c_5A^2B + c_6AB^2 + c_7A^3 + c_8B^3 + c_{10}A^2B^2 + c_{11}A^3B \\ & + c_{12}AB^3 + c_{13}A^4 + c_{13}B^4 + c_{14}A^3B^2 + c_{15}A^2B^3 + c_{15}A^4B + c_{16}AB^4 + c_{17}A^5 + c_{17}B^5 + c_{18}A^3B^3 \\ & + c_{19}A^4B^2 + c_{20}A^2B^4 + c_{21}A^5B + c_{22}AB^5 + c_{23}A^6 + c_{24}B^6 \end{aligned} \tag{3}$$

It should be noted that not all the terms must be present in the models. In fact, only terms with $p \leq 0.1$ were included, while the model was considered significant with a $p \leq 0.05$. The model function (indicated in the equation as *f*) was chosen (i) to normalize the model residues and (ii) to make the model residues pattern less. To evaluate the goodness of fit of the model, the coefficient of determination (R^2) was calculated.

Tensile testing

Specimens were tested uniaxially with a universal tensile testing machine (model 3365, Instron, USA), equipped with a 500 N load cell. Specimens of approximately $40 \times 10 \times 1$ mm (length × width × thickness) were printed using an infill pattern featuring parallel strands oriented either along the length or width of the rectangle. Specimens underwent tensile loading at a strain rate of 0.03 min^{-1}. The cross-section of each specimen was measured via optical microscopy and used to calculate the stress *vs.* strain curve, under the hypothesis of negligible necking. A typical stress–strain curve is reported in Supplementary fig. S2. The slope of the linear portion of the stress *vs.* strain curve was retrieved via Origin software (OriginLab Corp., USA) and used to estimate the Young's modulus of each specimen. Measurements were performed in triplicate. For the evaluation under cyclic stress, 100 loading–unloading cycles were performed on $OCB_{\perp}$ for a maximum elongation of 0.25%.

Preparation of conductive and electroluminescent formulations

E-OCB was prepared starting from OCB by adding selected amounts of Super P carbon black (Imerys Graphite & Carbon, France; 0.1 to 5 wt%), followed by planetary mixing (1 min) and degassing (30 s). Specimens with a square cross-section of approx. $40 \times 1 \times 1$ mm were extruded and dried in open air at 50 °C. Afterwards, four-terminals conductivity tests were performed using a SP-300 potentiostat/galvanostat (BioLogic, France), with power terminals connected to the specimen edges and sensing terminals placed at a distance of 1 mm, in the central portion of the specimen (Fig. 2b). A linear sweep voltammetry (LSV) was performed in the range 0 – 1 V. The slope of the linear portion of the voltage *vs.* current curve was used to retrieve the resistance of each sample; subsequently, specimens were cut in their central

portion and the area of the section was measured to precisely calculate material conductivity.

Conductivity values as a function of carbon black content were interpreted considering the statistical percolation theory (Bauhofer and Kovacs 2009):

$$\sigma = \sigma_0 \left(\chi - \chi_c\right)^t \text{for} \chi > \chi_c \quad (4)$$

where σ is the overall conductivity, σ_0 is the intrinsic conductivity of the conductive phase, χ is the weight fraction of the conductive phase in the composite, χ_c is the percolation threshold, and t is the critical exponent depending on the system dimensionality.

L-OCB samples were prepared by supplementing OCB with 20 wt% ZnS-based electroluminescent crystals (ProChima, Italy) under planetary mixing for 1 min, followed by 30 s degassing. Square specimens, approx. 15 mm × 15 mm × 2 mm, were printed and dried in a confined environment at 50 °C till complete dehydration.

In the case of composite devices, a first OCB layer (20 mm × 20 mm × 1 mm) was printed, followed by the extrusion of two 10-mm distant capacitor plate-like components with E-OCB (3 wt% carbon black), one layer of L-OCB filling the interspace between the E-OCB plates, and a final 20 mm × 20 mm × 1 mm OCB layer. Afterwards, the device was dried in a confined environment at 50 °C till complete dehydration.

For electroluminescence tests, L-OCB and composite devices were placed in a darkroom and connected to a high voltage DC generator (model ES30, Gamma High Voltage Research, USA).

Biocompatibility

Materials cytotoxicity was assessed according to ISO 10993–5. Briefly, sterile freeze-dried samples of OCB, P-OCB and E-OCB were immersed in complete cell culture medium (Eagle's MEM + 10% fetal bovine serum (FBS) + 1% penicillin/streptomycin + 1% L-glutamine) at a ratio of 0.1 g of material per mL of medium and incubated at 37 °C for 72 h. Then, the eluate was collected and used at three different titers (*i.e.*, (i) undiluted; (ii) 1:10; and (iii) 1:100 dilution in complete medium) to culture subconfluent human melanoma SK-MEL-2 cells (ATCC, USA) in a 96-well plate for 24 h (37 °C, 5% CO_2). Cytotoxicity was tested by MTT assay. Briefly, culture medium was replaced with 100 µL of 3-(4,5-dimethylthiazol-2-yl)-2,5-diphenyltetrazolium bromide solution (0.5 mg/ml in complete culture medium) and cells were incubated for four hours (37 °C, 5% CO_2). MTT solution was removed, formazan salts were dissolved in 100 µL of DMSO and quantified by measuring absorbance at λ = 595 nm on a plate reader (Infinite M200-Pro, Tecan, Austria). Cell viability was normalized to that of control (untreated) cells.

For 3D cell culture, freeze-dried OCB samples of approx. 5 × 5 × 3 mm (length x width x height) were sterilized by soaking in 70% ethanol, rinsed in sterile PBS and equilibrated in complete cell culture medium in a 24-well plate. Afterwards, cell culture medium was replaced with a SK-MEL-2 cells suspension (5×10^4 cells/scaffold) and cells were incubated for 2 h (37 °C, 5% CO_2). Constructs were then transferred in an empty well, fully covered with culture medium and incubated for 72 h. Constructs were then washed with PBS, fixed with 4% paraformaldehyde, and permeabilized with Triton X-100 (0.1% in PBS for 10 min). Actin was stained with Alexa Fluor 488 Phalloidin (1:500 in PBS, Thermo Fisher Scientific, USA) for 50 min and nuclei were counterstained with 5 µM Draq5 (abcam) in PBS for 30 min at RT. Given the significant autofluorescence of OCB in the 425 – 475 nm spectral range, a far-red fluorescent DNA dye was required to clearly visualize cell nuclei. Constructs were immersed in a 1:1 mixture of sucrose (30% in PBS) and Shandon Cryomatrix embedding resin (Thermo Scientific) at 4 °C overnight. Specimens were then included in pure Shandon Cryomatrix, snap frozen and sectioned (30 µm sections) with a Leica CM3050 S cryostat (Leica Biosystems, Germany). Confocal imaging was performed on a Nikon A1R + microscope, using excitation wavelengths of 405 nm, 561 nm and 647 nm, and emission ranges of 425–475 nm, 570–620 nm, and 650–700 nm, respectively.

Author's contribution Conceptualization, Methodology, Supervision: E.D.L., P.M., M.T., G.G., A.R.; Investigation: E.D.L., V.R., C.C., D.F.; Formal Analysis, Data Curation: A.B.; Visualization: E.D.L., A.B.; Writing—Original Draft: E.D.L.; Writing—Review & Editing: all authors; Resources and Funding acquisition: E.D.L., M.T., A.R.

Funding This work was funded by the European Union—Next Generation EU, Italian NRRP M4.C2—Investment 1.5 "Rome Technopole", CUP C83C22000510001. E.D.L. is supported by the Italian Ministry for University and

Research (Young Researchers—Seal of Excellence, CUP C83C22001250006). A.R. is granted by the Italian Ministry of Research, under the complementary actions to the NRRP "Fit-4MedRob—Fit for Medical Robotics" Grant (# PNC0000007). P.M. acknowledges the "National Center for Gene Therapy and Drug based on RNA Technology" (CN00000041 CN3 RNA), funded by the European Union—Next Generation EU – Italian NRRP M4.C2—Investment 1.4 (CUP B83C22002860006).

Data availability Data are available on request.

Declarations

Conflict of interests The authors declare no competing interests.

Human Ethics and Consent to Participate Not applicable.

References

Amela-Cortes M, Dumait N, Artzner F et al (2023) Flexible and transparent luminescent cellulose-transition metal cluster composites. Nanomaterials. https://doi.org/10.3390/nano13030580

BaşaranKankılıç G, Metin AÜ (2020) Phragmites australis as a new cellulose source: extraction, characterization and adsorption of methylene blue. J Mol Liq. https://doi.org/10.1016/j.molliq.2020.113313

Basu S, Omadjela O, Gaddes D et al (2016) Cellulose microfibril formation by surface-tethered cellulose synthase enzymes. ACS Nano 10:1896–1907. https://doi.org/10.1021/acsnano.5b05648

Bauhofer W, Kovacs JZ (2009) A review and analysis of electrical percolation in carbon nanotube polymer composites. Compos Sci Technol. https://doi.org/10.1016/j.compscitech.2008.06.018

Bossi AM, Bucciarelli A, Maniglio D (2021) Molecularly imprinted silk fibroin nanoparticles. ACS Appl Mater Interf 13:31431–31439. https://doi.org/10.1021/acsami.1c05405

Bucciarelli A, Olivetti E, Adami A, Lorenzelli L (2021) Design of experiment rational optimization of an inkjet deposition of silver on Kapton. IEEE Sens J 21:26304–26310. https://doi.org/10.1109/JSEN.2021.3058543

Bucciarelli A, Adami A, Chandaiahgari CR, Lorenzelli L (2020) Multivariable optimization of inkjet printing process of Ag nanoparticle ink on Kapton. In: 2020-IEEE International Conference on Flexible and Printable Sensors and Systems 3–6

Fang Z, Zhang H, Qiu S et al (2021) Versatile wood cellulose for biodegradable electronics. Adv Mater Technol 6:13–16. https://doi.org/10.1002/admt.202000928

Ferrer A, Salas C, Rojas OJ (2016) Physical, thermal, chemical and rheological characterization of cellulosic microfibrils and microparticles produced from soybean hulls. Ind Crops Prod 84:337–343. https://doi.org/10.1016/j.indcrop.2016.02.014

Fu X, Wang JK, Ramírez-Pérez AC et al (2020) Flexible conducting polymer-based cellulose substrates for on-skin applications. Mater Sci Eng C. https://doi.org/10.1016/j.msec.2019.110392

Gaiardo A, Novel D, Scattolo E et al (2021) Dataset of the optimization of a low power chemoresistive gas sensor: Predictive thermal modelling and mechanical failure analysis. Sensors. https://doi.org/10.3390/data6030030

Gori M, Giannitelli SM, Torre M et al (2020) Biofabrication of hepatic constructs by 3D bioprinting of a cell-laden thermogel: an effective tool to assess drug-induced hepatotoxic response. Adv Healthc Mater 9:1–11. https://doi.org/10.1002/adhm.202001163

Hausmann MK, Siqueira G, Libanori R et al (2020) Complex-shaped cellulose composites made by wet densification of 3D printed scaffolds. Adv Funct Mater. https://doi.org/10.1002/adfm.201904127

Hickey RJ, Pelling AE (2019) Cellulose biomaterials for tissue engineering. Front Bioeng Biotechnol. https://doi.org/10.3389/fbioe.2019.00045

Iglesias-Mejuto A, Malandain N, Ferreira-Gonçalves T et al (2024) Cellulose-in-cellulose 3D-printed bioaerogels for bone tissue engineering. Cellulose 31:515–534. https://doi.org/10.1007/s10570-023-05601-1

Illa MP, Sharma CS, Khandelwal M (2019) Tuning the physiochemical properties of bacterial cellulose: effect of drying conditions. J Mater Sci 54:12024–12035. https://doi.org/10.1007/s10853-019-03737-9

Imai M, Akiyama K, Tanaka T, Sano E (2010) Highly strong and conductive carbon nanotube/cellulose composite paper. Compos Sci Technol 70:1564–1570. https://doi.org/10.1016/j.compscitech.2010.05.023

ISO (2003) 10993–5 Biological evaluation of medical devices. In: Tests for in vitro cytotoxicity

Jain K, Wang Z, Garma LD et al (2023) 3D printable composites of modified cellulose fibers and conductive polymers and their use in wearable electronics. Appl Mater Today. https://doi.org/10.1016/j.apmt.2022.101703

Jonoobi M, Harun J, Mathew AP, Oksman K (2010) Mechanical properties of cellulose nanofiber (CNF) reinforced polylactic acid (PLA) prepared by twin screw extrusion. Compos Sci Technol 70:1742–1747. https://doi.org/10.1016/j.compscitech.2010.07.005

Jung YH, Chang TH, Zhang H et al (2015) High-performance green flexible electronics based on biodegradable cellulose nanofibril paper. Nat Commun. https://doi.org/10.1038/ncomms8170

Kuzmenko V, Karabulut E, Pernevik E et al (2018) Tailor-made conductive inks from cellulose nanofibrils for 3D printing of neural guidelines. Carbohydr Polym 189:22–30. https://doi.org/10.1016/j.carbpol.2018.01.097

Kwon H, Park S, Kwon S, Lee HT (2023) Effect of the cellulose nanofiber on ultraviolet curable resin for additive manufacturing: Mechanical properties and printability. Addit Manuf 78:103879. https://doi.org/10.1016/J.ADDMA.2023.103879

Lechner A, Trossmann VT, Scheibel T (2022) Impact of cell loading of recombinant spider silk based bioinks on gelation and printability. Macromol Biosci. https://doi.org/10.1002/mabi.202100390

Li VCF, Kuang X, Mulyadi A et al (2019) 3D printed cellulose nanocrystal composites through digital light processing. Cellulose 26:3973–3985. https://doi.org/10.1007/s10570-019-02353-9

Li Z, Wang F, Liu L et al (2022) Highly sensitive, breathable and durable E-textiles integrated by graphene ink via scalable aerodynamics assisted screen printing. Cellulose 29:4661–4671

Liu H, Quan J, Wang J et al (2023) Low delay flexible paper-based electrode for capacitive sensor filled through carbon-based materials. Cellulose. https://doi.org/10.1007/s10570-022-04951-6

Maturi M, Spanu C, Fernández-Delgado N et al (2023) Fatty acid: functionalized cellulose nanocomposites for vat photopolymerization. Addit Manuf 61:103342. https://doi.org/10.1016/J.ADDMA.2022.103342

Moon RJ, Martini A, Nairn J et al (2011) Cellulose nanomaterials review: structure, properties and nanocomposites. Chem Soc Rev 40:3941–3994. https://doi.org/10.1039/c0cs00108b

Nechyporchuk O, Belgacem MN, Pignon F (2016) Current progress in rheology of cellulose nanofibril suspensions. Biomacromol 17:2311–2320

Nishiyama Y (2009) Structure and properties of the cellulose microfibril. J Wood Sci 55:241–249. https://doi.org/10.1007/s10086-009-1029-1

Panaitescu DM, Donescu D, Bercu C et al (2007) Polymer composites with cellulose microfibrils. Polym Eng Sci. https://doi.org/10.1002/pen

Park JS, Kim T, Kim WS (2017) Conductive cellulose composites with low percolation threshold for 3D printed electronics. Sci Rep. https://doi.org/10.1038/s41598-017-03365-w

Pinto RJB, Carlos LD, Marques PAAP et al (2014) An overview of luminescent bio-based composites. J Appl Polym Sci. https://doi.org/10.1002/app.41169

Pokhrel S, Giri J, Kafle BP et al (2023) Preparation of electrically conducting bamboo paper using multi-walled carbon nanotubes. Macromol Symp. https://doi.org/10.1002/masy.202200131

Saleh AK, El-Sayed MH, El-Sakhawy MA et al (2024) Cellulose-based conductive materials for bioelectronics. Chemsuschem. https://doi.org/10.1002/cssc.202401762

Salehi MH, Golbaten-Mofrad H, Jafari SH et al (2021) Electrically conductive biocompatible composite aerogel based on nanofibrillated template of bacterial cellulose/polyaniline/nano-clay. Int J Biol Macromol 173:467–480. https://doi.org/10.1016/j.ijbiomac.2021.01.121

Schneider CA, Rasband WS, Eliceiri KW (2012) NIH Image to ImageJ: 25 years of image analysis. Nat Methods 9(7):671–675. https://doi.org/10.1038/nmeth.2089

Sehaqui H, Zhou Q, Berglund LA (2011) Nanostructured biocomposites of high toughness: a wood cellulose nanofiber network in ductile hydroxyethylcellulose matrix. Soft Matter 7:7342–7350. https://doi.org/10.1039/c1sm05325f

Shafiei-Sabet S, Hamad WY, Hatzikiriakos SG (2012) Rheology of nanocrystalline cellulose aqueous suspensions. Langmuir 28:17124–17133. https://doi.org/10.1021/la303380v

Shi C, Hou X, Li X, Ge M (2017) Preparation and characterization of persistent luminescence of regenerated cellulose fiber. J Mater Sci: Mater Electron 28:1015–1021. https://doi.org/10.1007/s10854-016-5622-y

Siqueira G, Kokkinis D, Libanori R et al (2017) Cellulose nanocrystal inks for 3D printing of textured cellular architectures. Adv Funct Mater. https://doi.org/10.1002/adfm.201604619

Small AC, Johnston JH (2008) Novel hybrid materials of cellulose fibres and doped ZnS nanocrystals. Curr Appl Phys 8:512–515. https://doi.org/10.1016/j.cap.2007.10.046

Torvinen K, Pettersson F, Lahtinen P et al (2017) Nanoporous kaolin: cellulose nanofibril composites for printed electronics. Flexible Printed Electron 2:24004. https://doi.org/10.1088/2058-8585/aa6d97

Turbak AF, Snyder FW, Sandberg KR (1983) Microfibrillated cellulose, a new cellulose product: properties, uses, and commercial potential. J Appl Polym Sci Appl Polym Symp 37:815–827

Wang L, Hu S, Ullah MW et al (2020) Enhanced cell proliferation by electrical stimulation based on electroactive regenerated bacterial cellulose hydrogels. Carbohydr Polym. https://doi.org/10.1016/j.carbpol.2020.116829

Xu X, Zhou J, Jiang L et al (2016) Highly transparent, low-haze, hybrid cellulose nanopaper as electrodes for flexible electronics. Nanoscale 8:12294–12306. https://doi.org/10.1039/C6NR02245F

Yang Z, Chen S, Hu W et al (2012) Flexible luminescent CdSe/bacterial cellulose nanocomoposite membranes. Carbohydr Polym 88:173–178. https://doi.org/10.1016/j.carbpol.2011.11.080

Yang L, Meng J, Xue T et al (2024) Application of 3D printing cellulose fabrics based on cotton fibers in the textile and fashion industry. Addit Manuf 81:104000. https://doi.org/10.1016/J.ADDMA.2024.104000

Zhao D, Zhu Y, Cheng W et al (2021) Cellulose-based flexible functional materials for emerging intelligent electronics. Adv Mater. https://doi.org/10.1002/adma.202000619

Zheng Q, Li H, Zheng Y et al (2021) Cellulose-based flexible organic light-emitting diodes with enhanced stability and external quantum efficiency. J Mater Chem C 9:4496–4504. https://doi.org/10.1039/D1TC00019E

Zhong C (2020) Industrial-scale production and applications of bacterial cellulose. Front Bioeng Biotechnol 8:1–19. https://doi.org/10.3389/fbioe.2020.605374